

This is the accepted manuscript made available via CHORUS. The article has been published as:

# Topological limit of ultrathin quasi-free-standing $\text{Bi}_{\{2\}}\text{Te}_{\{3\}}$ films grown on Si(111)

Yang Liu, Guang Bian, T. Miller, Mark Bissen, and T.-C. Chiang

Phys. Rev. B **85**, 195442 — Published 22 May 2012

DOI: [10.1103/PhysRevB.85.195442](https://doi.org/10.1103/PhysRevB.85.195442)

# Topological Limit of Ultrathin Quasi-freestanding $\text{Bi}_2\text{Te}_3$ Films Grown on Si(111)

Yang Liu<sup>1,2</sup>, Guang Bian<sup>1,2</sup>, T. Miller<sup>1,2</sup>, Mark Bissen<sup>3</sup> & T.-C. Chiang<sup>1,2,3</sup>

<sup>1</sup>Department of Physics, University of Illinois at Urbana-Champaign, 1110 West Green Street,  
Urbana, Illinois 61801-3080, USA

<sup>2</sup>Frederick Seitz Materials Research Laboratory, University of Illinois at Urbana-Champaign,  
104 South Goodwin Avenue, Urbana, Illinois 61801-2902, USA

<sup>3</sup>Synchrotron Radiation Center, University of Wisconsin-Madison, 3731 Schneider Drive,  
Stoughton, WI 53589-3097, USA

A fundamental issue for ultrathin topological films is the thickness limit below which the topological surface states become impacted by interfacial interaction. We show that for  $\text{Bi}_2\text{Te}_3$  grown on Si(111) this limit is 4 quintuple layers based on angle-resolved photoemission measurements, using optimized photon energies and polarizations, of the Dirac cone warping and interaction-induced gap as a function of film thickness. The results are close to theoretical predictions for freestanding films. Evidence is presented to show why the substrate-film interaction is actually weak.

PACS numbers:      73.20-r      73.22-f      73.61-Ng

## I. INTRODUCTION

Topological insulators are promising materials for spintronic device applications; their bulk symmetry properties guarantee that the bulk gap is spanned by spin-polarized surface states that are well suited for spin transport [1,2,3,4]. For device architecture based on massive integration, ultrathin films are ideal building blocks. Additional benefits of a minimal film thickness include: (1) bulk conduction and scattering caused by natural defects, a common problem, is minimized [5,6,7,8]; (2) the band gap can be substantially enhanced by quantum size effects, allowing wider device operational ranges; and (3) discretization of the bulk bands can make a semimetal, or even a metal, an insulator or a poor metal with few bulk conducting channels, thus substantially broadening the choices of available materials. However, the useable film thickness has a natural lower limit, below which interactions between the two film boundaries can open up a gap at the Dirac point, cutting off the spin conduction.

$\text{Bi}_2\text{Te}_3$  is a strong topological insulator, whose spin-polarized topological surface states (TSSs) form a single Dirac cone at the zone center [9,10,11,12]. Recently, high-quality ultrathin  $\text{Bi}_2\text{Te}_3$  and  $\text{Bi}_2\text{Se}_3$  films were successfully grown by molecular beam epitaxy (MBE) and measured by angle-resolved photoemission spectroscopy (ARPES) using He discharge sources [13,14]. While the gap opening of TSSs in  $\text{Bi}_2\text{Se}_3$  films was observed below 6 quintuple layers (QLs) [14], no clear evidence for such effects has been reported for  $\text{Bi}_2\text{Te}_3$  [13]. Our work using ARPES under carefully chosen experimental conditions shows a much smaller critical thickness of just 4 QL for  $\text{Bi}_2\text{Te}_3$  grown on  $\text{Si}(111)-(7\times 7)$ , which is in excellent agreement with theoretical predictions for freestanding films [15,16,17]. The results indicate a very weak film-substrate interaction, a surprising outcome in view of the expected strong interfacial bonding involving the Si dangling bonds. Our calculations suggest that a strong film-substrate interaction could actually

help achieve the ultimate “bulkless” thickness limit of 2 QLs where the gapless configuration of the TSSs is preserved.

## II. EXPERIMENTAL AND COMPUTATIONAL DETAILS

Our ARPES measurements were performed at the Synchrotron Radiation Center (SRC), University of Wisconsin-Madison. The data in Fig. 1(b) and Figs. 4(c) and 4(d) were taken at 20 K, using a Scienta SES200U analyzer at the new U9 PGM-VLS beamline. All the other data were taken at 60 K, using a Scienta SES100 analyzer at the U-NIM beamline. The energy and momentum resolutions were 20 meV and  $0.01 \text{ \AA}^{-1}$ , respectively.  $\text{Bi}_2\text{Te}_3$  films were prepared by depositing Te and Bi simultaneously, with a flux ratio ( $\theta$ ) of about 4, onto clean Si(111)-(7x7) held at  $\sim 300 \text{ }^\circ\text{C}$  [13]. The film thickness was determined by a crystal thickness monitor and by layer counting from the discrete evolution of the quantum well states (QWSs). Our first-principles calculations were performed under the local-density approximation within the density functional theory framework using the ABINIT program [18]. The lattice constants are adopted from a previous study [19].

## III. RESULTS AND DISCUSSION

### A. SAMPLE CHARACTERIZATION

Figure 1(a) shows a reflection high-energy electron diffraction (RHEED) pattern from a 4-QL film; the sharp  $1 \times 1$  pattern indicates a smooth film. The measured in-plane lattice constant,  $4.36 \pm 0.04 \text{ \AA}$ , agrees with the known bulk value of  $4.383 \text{ \AA}$ . Spectra from Te 4d and Bi 5d core levels (Fig. 1(b)) are consistent with those measured from cleaved samples [20]; the opposite energy shifts relative to bulk Te and Bi prepared as thick films are caused by the partially ionic

bonding between Bi and Te. The condition for stoichiometric growth is verified by the invariance of the ARPES spectra to the Te flux (Fig. 1(c)); it is known that high-quality  $\text{Bi}_2\text{Te}_3$  films can be readily grown in a Te-rich environment [13]. The various spectral features seen in Fig. 1(c) can be enhanced or suppressed by varying the photon energy because of variations of the photoemission cross sections. ARPES data and the resulting dispersion relations for a 5-QL film are shown in Fig. 1(d); TSSs, QWSs derived from the valence bands, and a feature derived from the conduction band (CB) are indicated. While the relative ARPES intensities of these features vary, the energy positions stay fixed as a function of photon energy. The results confirm the two-dimensional nature of the observed states. The lower TSS, as it moves away from the zone center, soon encounters the valence band region and evolves into a QWS.

The evolution of TSSs as a function of momentum is illustrated in Fig. 2, which shows the calculated band dispersions for a 6-QL freestanding film, together with the plane-averaged charge densities at several representative points (A-F), as indicated in Fig. 2(b). The TSSs form a Dirac point at  $\bar{\Gamma}$  just slightly above the valence band edge. They disperse with increasing  $k_x$  and move into the conduction and valence band regions (shaded regions) where they become QWSs. States A, D, and E, which are within the bulk gap, are strongly localized near the surface. The other states B, C, F and G have more diffuse wave functions characteristic of QWSs.

## B. HEXAGONAL WARPING OF TOPOLOGICAL SURFACE STATES

The distinction between QWSs and TSSs is made clear by measuring the dependence of the dispersion relations on film thickness (Fig. 3(a)). The spectra show nearly the same CB and TSS features, while the QWSs with energies between about  $-0.4$  to  $-0.6$  eV split into more subbands as the film thickness increases from 2 to 5 QLs. These layer-resolved QWSs provide a

means to accurately calibrate the exact thickness of each film [21]. The quantization of the CB is not observed experimentally, because most of CB lies above the Fermi level. The V-shaped upper TSS band shows two nearly linear branches at 2 QLs, but each branch develops a kink at about  $-0.15$  eV for thicker films. This effect is more easily seen in the constant-energy contours (Fig. 3(b)), where the left panels display the original data at  $0.28$  eV above the Dirac point ( $E_D \approx -0.4$  eV), and the right panels display the results of a best fit overlaid on the data. The contour appears as a hexagon at 2 QL but evolves into a snowflake-like shape at higher thicknesses. This evolution, known as the hexagonal warping effect, can be attributed to band structure development as the film gets thicker [9,22,23]. The fitting is based on the model function [22]:

$$E(\mathbf{k}) = E_0(\mathbf{k}) + \sqrt{v_k^2 k^2 + \lambda^2 k^6 \cos^2(3\phi)}, \quad (1)$$

where  $E$  and  $\mathbf{k}$  denote the energy and wave vector of the TSS state,  $v$  is the electronic group velocity,  $\lambda$  describes the strength of the crystal potential,  $\phi$  is the azimuth angle of  $\mathbf{k}$  with respect to the  $\bar{\Gamma}\bar{K}$  direction, and  $E_0$  is a free-electron-like dispersion function. The fits (green curves in Fig. 3(b)) describe the data well. The fitting parameter,  $\lambda/v$ , determines the warping. It increases for increasing film thickness from 2 to 4 QLs but saturates at larger thicknesses (Fig. 3(c)). This asymptotic behavior suggests that beyond the 4-QL critical thickness the TSS no longer senses the presence of the interface; or, the system has become bulklike for the TSS. A further test is that the experimental warping factor, defined as the ratio between the wave vectors along the  $\bar{\Gamma}\bar{K}$  and  $\bar{\Gamma}\bar{M}$  directions, is consistent with the bulk limit determined previously (Fig. 3(d)) [9,24]. Our experimental results also agree well with first-principles calculations in terms of the asymptotic behavior (Fig. 3(d)), but the numerical values differ, possibly due to inaccuracies in the band calculations.

### C. GAP OPENING AT $\bar{\Gamma}$

A key property of TSSs is that they connect the valence and conduction bands resulting in a metallic surface. However, when the film thickness is reduced to the order of the decay length of the TSSs, degenerate coupling (or quantum tunneling) of the TSSs at the two film boundaries can give rise to an energy gap at the Dirac point [14]. A gap of 0.14 eV is evident at 2 QL (Fig. 4(b)), but it becomes much smaller at 3 QL and beyond. To determine the gap at different film thicknesses, we exploit the strong dependence of the photoemission cross sections on the incident light polarization (Fig. 4(c)). Figure 4(a) shows two different polarization configurations employed: horizontal (HP or  $p$ ) and vertical polarization (VP or  $s$ ). Because the allowed photoemission final states near normal emission must have an even parity in the  $x$ - $y$  plane,  $p$ - and  $s$ - polarized light mainly excites electronic states with even and odd parity, respectively. As seen in Fig. 4(c), the emission from the states below the Dirac point is strong for  $p$ -polarization and much weaker for  $s$ -polarization. This behavior is in agreement with the mainly  $p_z$  character of the valence bands [11,25,26]. When a gap opens up in the TSSs, the lower branch, in close proximity to the valence band edge, mostly possesses a similar  $p_z$  character. On the other hand, the emission from the V-shaped upper branch shows a very different polarization dependence because of its true surface character and a strong spin-orbit coupling [16]. The large variations in the relative ARPES intensities facilitate a determination of the gap size, even though the two peaks are not necessarily resolved in individual spectra at larger film thicknesses (Fig. 4(d)). As illustrated in Fig. 4(d), the  $p$ - or  $s$ -polarized light predominantly excites one or the other TSS; the energy difference between the peaks corresponds to the gap for each thickness. By contrast, the peak at about  $-0.1$  eV, corresponding to a conduction band feature, has a position independent of the polarization configuration. The gaps are further confirmed by a least-

squares fitting analysis of spectra taken over a wide range of photon energy. An example is presented in Fig. 5 for the 3-QL film; the relative photoemission intensities are different for the different spectra, and the fits are carried out simultaneously for all spectra. The extracted gap values for different film thicknesses, shown in Fig. 4(e) with error bars representing experimental uncertainties, approximately follow an exponential decay in excellent agreement with first-principles calculations for freestanding films [15,16,17].

#### D. EVIDENCES FOR QUASI-FREESTANDING FILMS

The good agreement in measured gap values with calculations of freestanding slabs is surprising and implies that the films are quasi-freestanding. The substrate surface, Si(111)-(7x7), is chemically active because of the presence of dangling bonds [27]. Strong chemical bonding at the Bi<sub>2</sub>Te<sub>3</sub>-Si interface would be expected to substantially modify the TSSs at the interface, thus removing the degenerate coupling responsible for the gap formation at the Dirac point [28]. Indeed, first-principles calculations of Bi<sub>2</sub>Te<sub>3</sub> films with the bottom surface terminated by atomic hydrogen show no gap opening for the TSSs on the top surface over the thickness range of 2-5 QLs (Fig. 6). Hydrogen termination is a standard theoretical model for interfacial chemical bonding. In the present case, it should approximately describe the effects of the bonding of the film to the Si substrate [29]; however, the results are inconsistent with the experimental observation.

This puzzling behavior is explained by a Te wetting or buffer layer on the Si(111) surface that saturates all of the Si(111) dangling bonds, resulting in an effective isolation of the subsequently grown Bi<sub>2</sub>Te<sub>3</sub> overlayer from direct chemical bonding to the Si and thus making the film quasi-freestanding. Evidence for this buffer layer can be deduced from RHEED, ARPES,



and prior STM measurements [30,31]. Under a Te-rich growth condition, the Si(111)-(7x7) surface is quickly saturated by Te. RHEED patterns (Fig. 7(a)) show that after exposing the Si surface to about 1 monolayer of Te most of the (7x7) features disappear. Strong (1x1) spots remain together with very weak nearest 1/7 satellite peaks. Simultaneously, the surface states of Si(111)-(7x7), labeled S1, S2 and S3 in Fig. 7(a), are quenched and replaced by new surface states S4 and S5. The quenching of S1, S2 and S3 indicates the removal of Si dangling bonds. The remnant 1/7 satellite diffraction peaks indicate that the (7x7) modulation remains [32]. Further co-deposition of Bi and Te on the Te-terminated surface results in the growth of Bi<sub>2</sub>Te<sub>3</sub> films one QL at a time, as evidenced by the ARPES results taking along the  $\bar{\Gamma}\bar{K}$  direction (Fig. 7(b)) and the emergence of the Bi<sub>2</sub>Te<sub>3</sub> diffraction pattern (Fig. 7(a)).

The Te-buffer-layer-capped Si surface shows little ARPES intensity above about -1.1 eV (Fig. 7(a)); thus, the Fermi level is pinned near the conduction band edge of the Si substrate due to the N-type surface doping by the Te. The new surface states S4 and S5 are located below the valence band edge of Si. The large band gap of Si, 1.1 eV, ensures that the TSSs on the interface side of the Bi<sub>2</sub>Te<sub>3</sub> overlayer experience little electronic interaction with the substrate. The result is an electronic structure very close to that of a freestanding Bi<sub>2</sub>Te<sub>3</sub> film. Similar electronic decoupling has been reported for Bi(001) films on Si(111) [33]. The slight asymmetry of the two film boundaries could induce a splitting of the TSSs into two sets, one associated with each surface; this splitting is not observed (Fig. 7(b)), indicating that the two surfaces of the film are nearly equivalent.

## IV. CONCLUDING REMARKS

Our work shows that ARPES measurements using optimally selected photon energies and polarization configurations for contrast enhancement constitute a powerful approach for an accurate determination of TSSs in topological insulator thin films. While our observed critical thickness of 4 QLs, verified by both the Dirac cone warping and the interaction-induced gap, is in close agreement with theory, previous studies of films of the related compound  $\text{Bi}_2\text{Se}_3$  have reported a substantially larger critical thickness of  $\sim 6$  QLs, where the discrepancy with theory is not yet fully understood [14,34]. The experimental realization of quasi-freestanding  $\text{Bi}_2\text{Te}_3$  films could provide opportunities to test some recent theoretical predictions for such films. One prediction is an enhanced thermoelectric response by gap opening [35]. Another prediction is a thickness-dependent oscillation of topological order [15,36,37]. Specifically, a freestanding 3-QL  $\text{Bi}_2\text{Te}_3$  film is possibly topologically trivial with a gap reversal compared to 2- and 4-QL films [15,37]. Our experimental results (Figs. 3, 4 and 5), while in good agreement with theory, do not directly reveal the nature of the gap. Other experimental probes (such as STM and transport) might be needed to clarify this issue.

The measured critical thickness of 4 QL for quasi-freestanding  $\text{Bi}_2\text{Te}_3$  films establishes an important design limit for nanoscale applications. Interestingly, this limit can be pushed further, based on our analysis of the H-terminated films, to the "bulkless" case of a 2-QL film (Fig. 4(e)) [28]. Thus, a strong chemical bonding at the interface can be beneficial, with implications of opportunities for interfacial engineering. Since the wave functions of the TSSs in  $\text{Bi}_2\text{Te}_3$  are essentially localized within just 1 QL, the 2-QL configuration represents the ultimate quantum limit for device architecture based on such nanofilms.

## **Acknowledgement**

This research was supported by the U.S. Department of Energy (grant DE-FG02-07ER46383). Y.L. thanks Haijun Zhang for helpful discussions. The Synchrotron Radiation Center is primarily funded by the University of Wisconsin-Madison with supplemental support from facility users and the University of Wisconsin-Milwaukee. We acknowledge the Petroleum Research Fund, administered by the American Chemical Society, and the U.S. National Science Foundation (grant DMR-09-06444) for partial support of the beamline facilities and operations.

## Reference

- [1] M. Z. Hasan, and C. L. Kane, Rev. Mod. Phys. **82**, 3045 (2010).
- [2] X.-L. Qi, and S.-C. Zhang, Rev. Mod. Phys. **83**, 1057 (2011).
- [3] J. E. Moore, Nature **464**, 194 (2010).
- [4] M. König *et al.*, Science **318**, 766 (2007).
- [5] H Peng *et al.*, Nature Mater. **9**, 225 (2010).
- [6] D. Kong *et al.*, Nature Nanotech. **6**, 705 (2011).
- [7] H. Steinberg, D. R. Gardner, Y. S. Lee and P. Jarillo-Herrero, Nano Lett. **10**, 5032 (2010).
- [8] F. Xiu *et al.*, Nature Nanotech. **6**, 216 (2011).
- [9] Y. L. Chen *et al.*, Science **325**, 178 (2009).
- [10] D. Hsieh *et al.*, Nature **460**, 1101 (2009).
- [11] H. Zhang *et al.*, Nature Phys. **5**, 438 (2009).
- [12] D. Hsieh *et al.*, Phys. Rev. Lett. **103**, 146401 (2009).
- [13] Y. Y. Li *et al.*, Adv. Mater. **22**, 4002 (2010).
- [14] Y. Zhang *et al.*, Nature Phys. **6**, 584 (2010).
- [15] C.-X. Liu *et al.*, Phys. Rev. B **81**, 041307 (R) (2010).
- [16] O. V. Yazyev, J. E. Moore, and S. G. Louie, Phys. Rev. Lett. **105**, 266806 (2010).
- [17] K. Park, J. J. Heremans, V. W. Scarola, and D. Minic, Phys. Rev. Lett. **105**, 186801 (2010).
- [18] X. Gonze *et al.*, *Computer Phys. Commun.* **180**, 2582 (2009).
- [19] W. Zhang, R. Yu, H.-J. Zhang, X. Dai, and Z. Fang, New J. Phys. **12**, 065013 (2010).
- [20] M. R. Scholz *et al.*, arXiv:1108.1037v1.

- [21] T.-C. Chiang, *Surf. Sci. Rep.* **39**, 181 (2000).
- [22] L. Fu, *Phys. Rev. Lett.* **103**, 266801 (2009).
- [23] Z. Alpichshev *et al.*, *Phys. Rev. Lett.* **104**, 016401 (2010).
- [24] S.-Y. Xu *et al.*, arXiv:1101.3985v1.
- [25] C. Jozwiak *et al.*, *Phys. Rev. B* **84**, 165113 (2011).
- [26] M. R. Scholz *et al.*, arXiv:1108.1053v1.
- [27] K. Takayanagi, Y. Tanishiro, M. Takahashi, and S. Takahashi, *J. Vac. Sci. Technol. A* **3** (3), 1502 (1985).
- [28] G. Bian, X. Wang, Y. Liu, T. Miller, and T.-C. Chiang, *Phys. Rev. Lett.* (accepted).
- [29] G. Bian, X. Wang, Y. Liu, T. Miller, and T.-C. Chiang, *Phys. Rev. B* **84**, 235414 (2011).
- [30] H. W. Liu *et al.*, *Crystal Growth & Design* **10** (10), 4491 (2010).
- [31] Y. Kanai, T. Yasue, and T. Koshikawa, *E-J. Surf. Sci. Nanotech.* **4**, 406 (2006).
- [32] R. D. Aburano *et al.*, *Phys. Rev. B* **52**, 1839 (1995).
- [33] T. Hirahara *et al.*, *Phys. Rev. Lett.* **97** 146803 (2006).
- [34] Y. Sakamoto, T. Hirahara, H. Miyazaki, S.-I. Kimura, and S. Hasegawa, *Phys. Rev. B* **81**, 165432 (2010).
- [35] P. Ghaemi, R. S. K Mong, and J. E. Moore, *Phys. Rev. Lett.* **105**, 166603 (2010).
- [36] J. Linder, T. Yokoyama, and A. Sudbo, *Phys. Rev. B* **80**, 205401 (2009).
- [37] H.-Z. Lu *et al.*, *Phys. Rev. B* **81**, 115407 (2010).

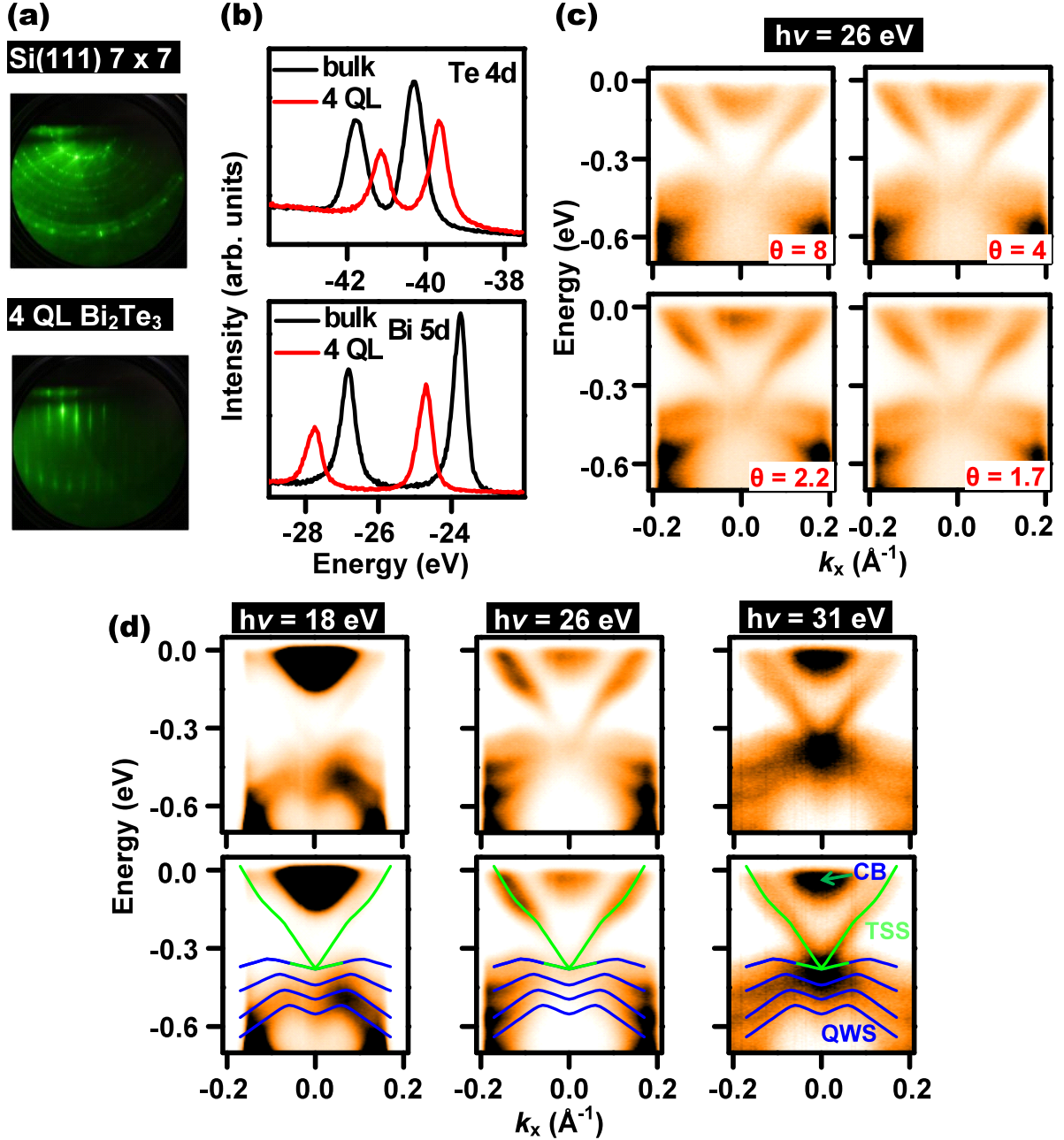


Fig. 1 (Color online). Sample characterization and 2D electronic states in  $\text{Bi}_2\text{Te}_3$  films. (a) RHEED images from the  $\text{Si}(111)-(7 \times 7)$  substrate and a 4-QL film with the incident electron beam along the  $\bar{\Gamma}\bar{K}$  direction. (b) Te 4d and Bi 5d core levels taken from a 4-QL film and bulk samples (thick films) of Te and Bi. The photon energies used are 65 and 55 eV, respectively. (c) Photoemission spectra of four 3.4-QL films grown under a fixed Bi flux and different Te:Bi flux ratios  $\theta$ . (d) Photoemission spectra of a 5-QL film taken along the  $\bar{\Gamma}\bar{M}$  ( $x$ ) direction at various photon energies. The bottom panels show the extracted dispersions overlaid on top of the data. The extracted dispersions are obtained by simultaneously fitting the peaks in the experimental data taken at various photon energies. Features CB, TSS and QWS correspond to the conduction band, topological surface states (green curves), and quantum well states (blue curves).

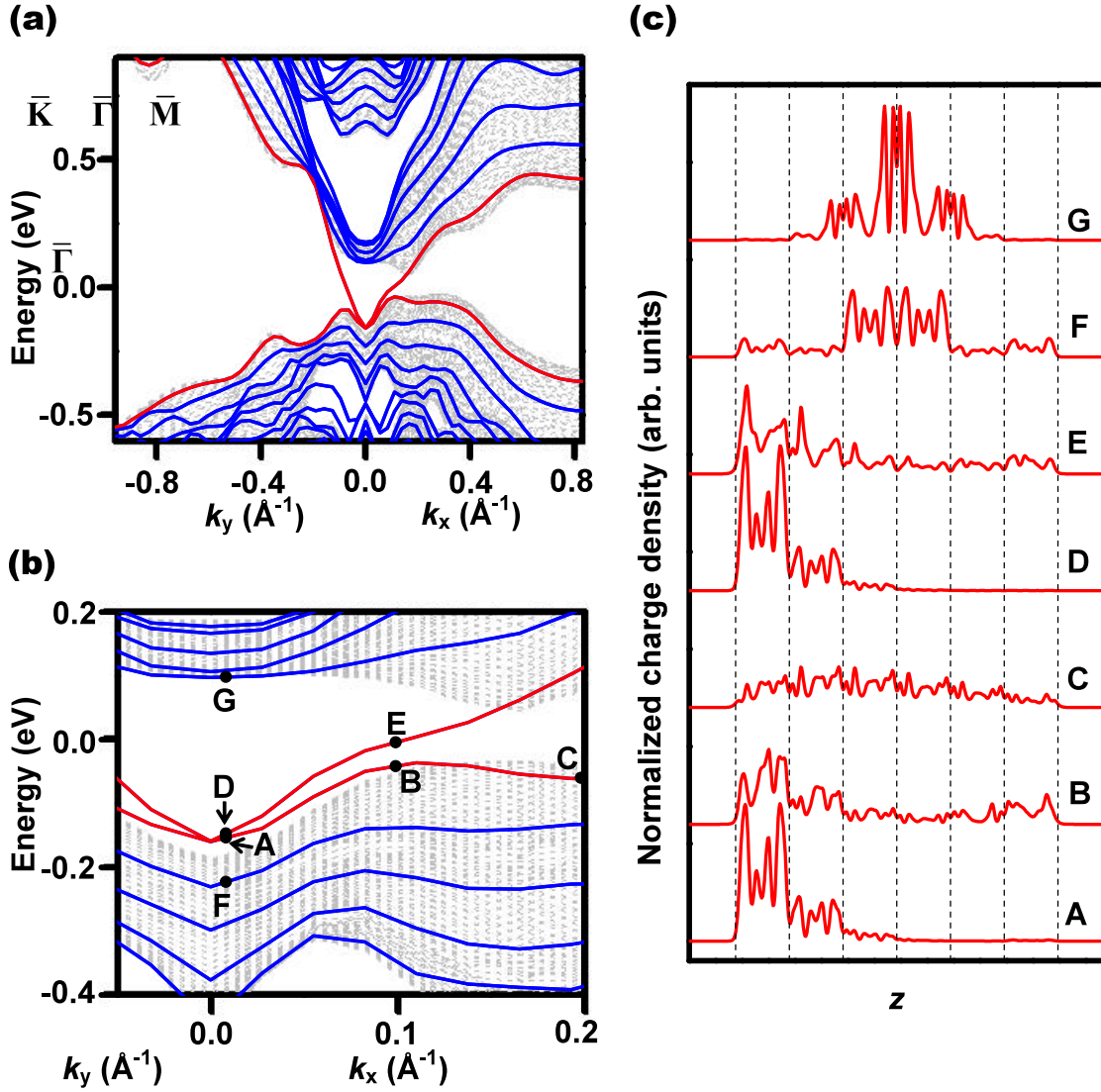


Fig. 2 (Color online). Band structure of a 6 QL freestanding  $\text{Bi}_2\text{Te}_3$  film from first-principles calculations. (a) Calculated band dispersion relations (curves) along two high symmetry directions. Red curves mark the topological surface states that smoothly connect the valence band and the conduction band. The shaded areas are projected bulk band regions. (b) Zoomed-in view of (a) near the Dirac point. (c) Normalized plane-averaged electronic charge density for states marked in (b). Vertical dashed lines mark the boundaries of the QLs.

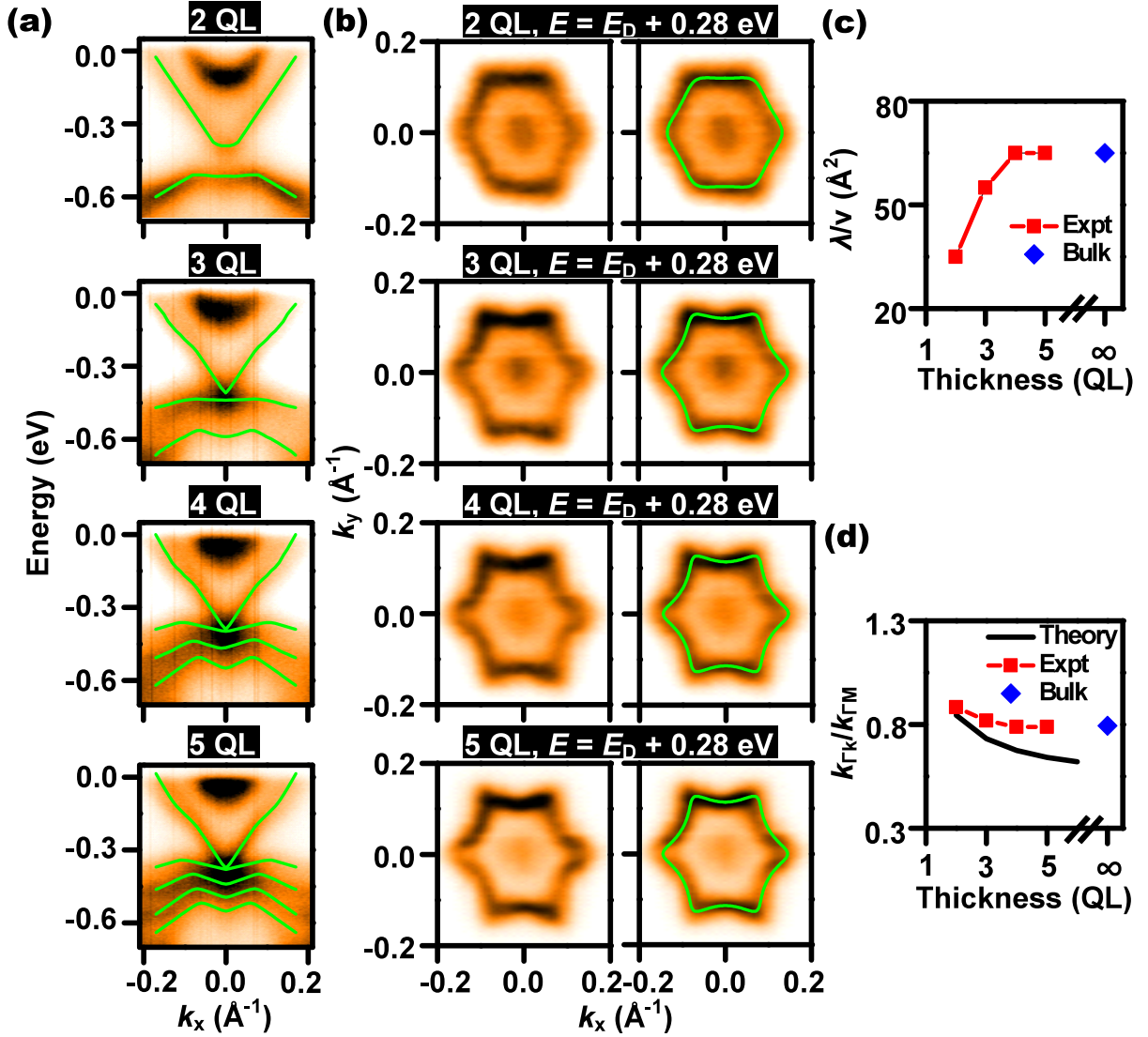


Fig. 3 (Color online). Electronic dispersion relations of Bi<sub>2</sub>Te<sub>3</sub> films as a function of thickness. (a) Photoemission spectra of 2- through 5-QL films measured along the  $\bar{\Gamma}\bar{M}$  direction, using 31-eV photons. Green curves are band dispersions extracted from data taken at various photon energies in a manner similar to that leading to Fig. 1(d) and Fig. 5. (b) Constant energy contours at 0.28 eV above the Dirac point for the same set of films, taken with 26-eV photons. Green curves are best fits to the experimental data. (c) Deduced fitting parameter  $\lambda/v$  from (b) for different film thicknesses. (d) Experimental warping factor at  $E = 0.28$  eV above the Dirac point, defined as the ratio between the wave vectors along  $\bar{\Gamma}\bar{K}$  and  $\bar{\Gamma}\bar{M}$ , compared with first-principles calculations for freestanding films. The bulk values in (c) and (d) are taken from an undoped Bi<sub>2</sub>Te<sub>3</sub> sample per Ref. [24].



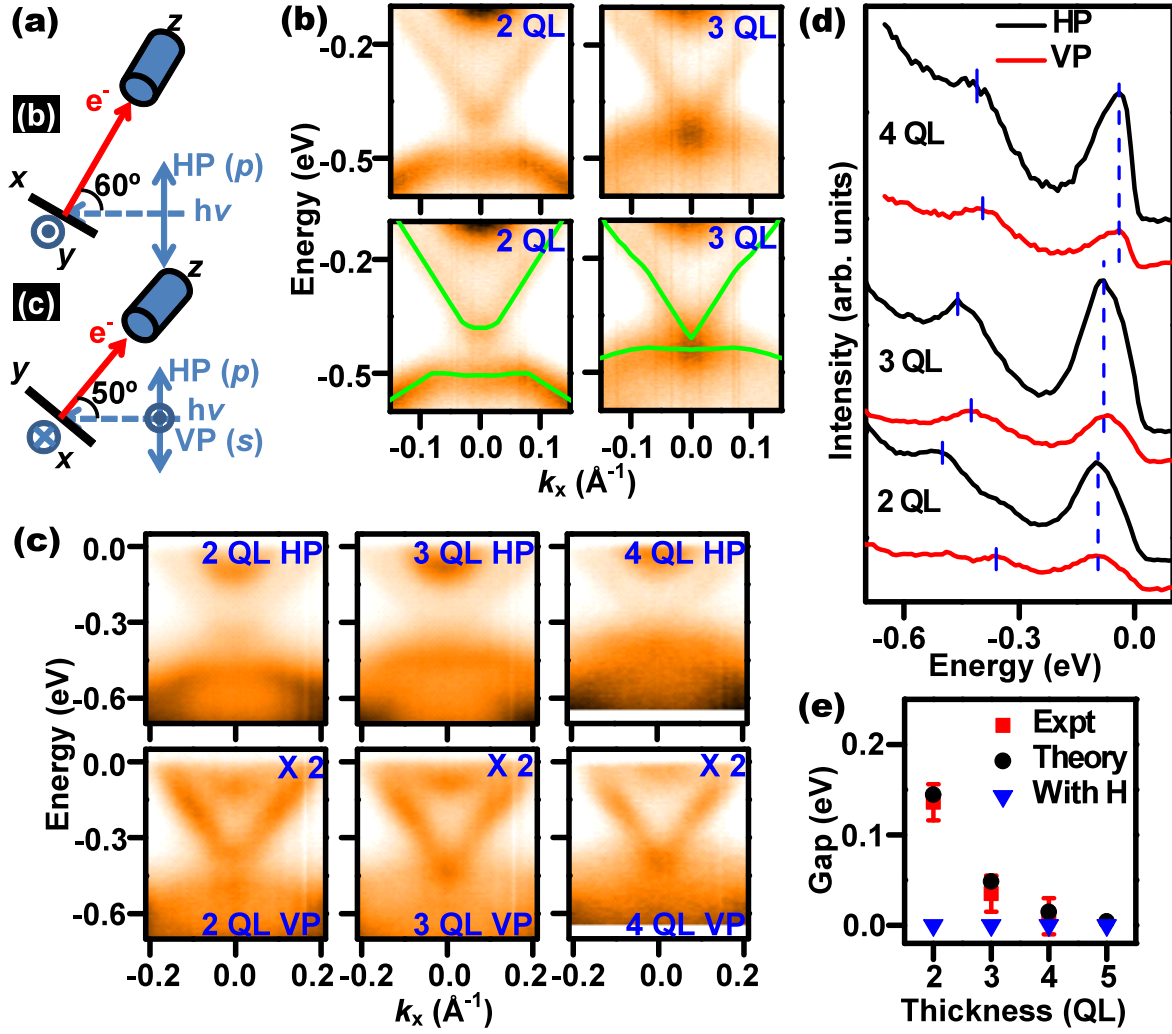


Fig. 4 (Color online). Extracting the gap at the Dirac point through polarization-dependent photoemission. (a) Schematic experimental configurations for the data presented in (b) and (c). (b) Photoemission spectra of 2- and 3-QL films using 31-eV photons with HP light. Green curves are extracted band dispersions (the details for 3 QL are shown in Fig. 5). (c) Photoemission spectra of 2- through 4-QL films using 28-eV photons with HP and VP light for comparison. The data taken with VP are amplified in intensity by a factor of 2. (d) Normal-emission plots for the data in (c). For spectra taken with HP (VP) light, the peak positions of the upper (lower) TSSs are marked by short vertical lines. The long vertical dashed lines denote the positions of the conduction band feature. (e) Deduced gap as a function of thickness (red squares with error bars), compared with first-principles calculations for freestanding films (black circles) and for films with the bottom side terminated by hydrogen (blue triangles).

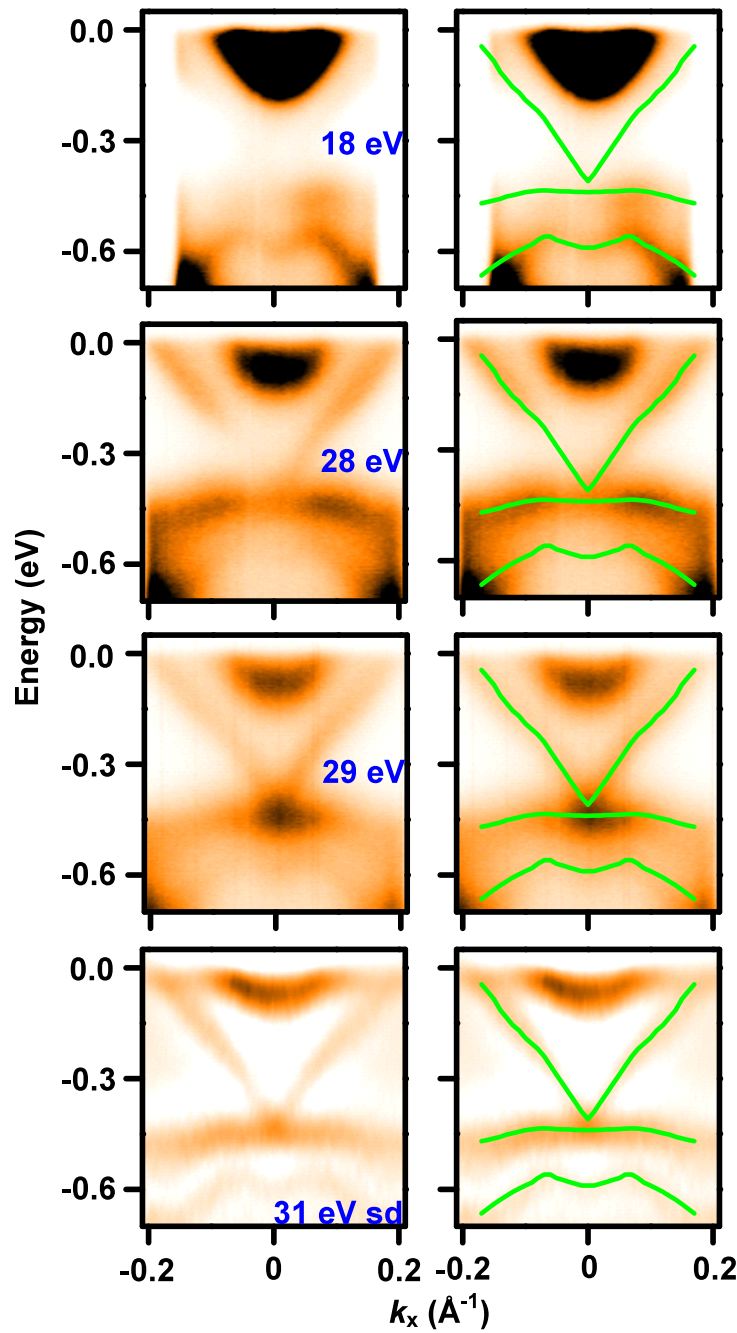


Fig. 5 (Color online). Extracting the band dispersion relations for a 3-QL film by simultaneously fitting the photoemission spectra taken at various photon energies as indicated. Left panels (from top to bottom): data taken at 18, 28, and 29 eV, and the second derivative (sd) of data taken at 31 eV. Certain portions of the bands are preferably excited by photons with specific energies, thus permitting a more accurate determination of the dispersion relations. Right panels: extracted band dispersion relations (green curves) overlaid on top of the data.

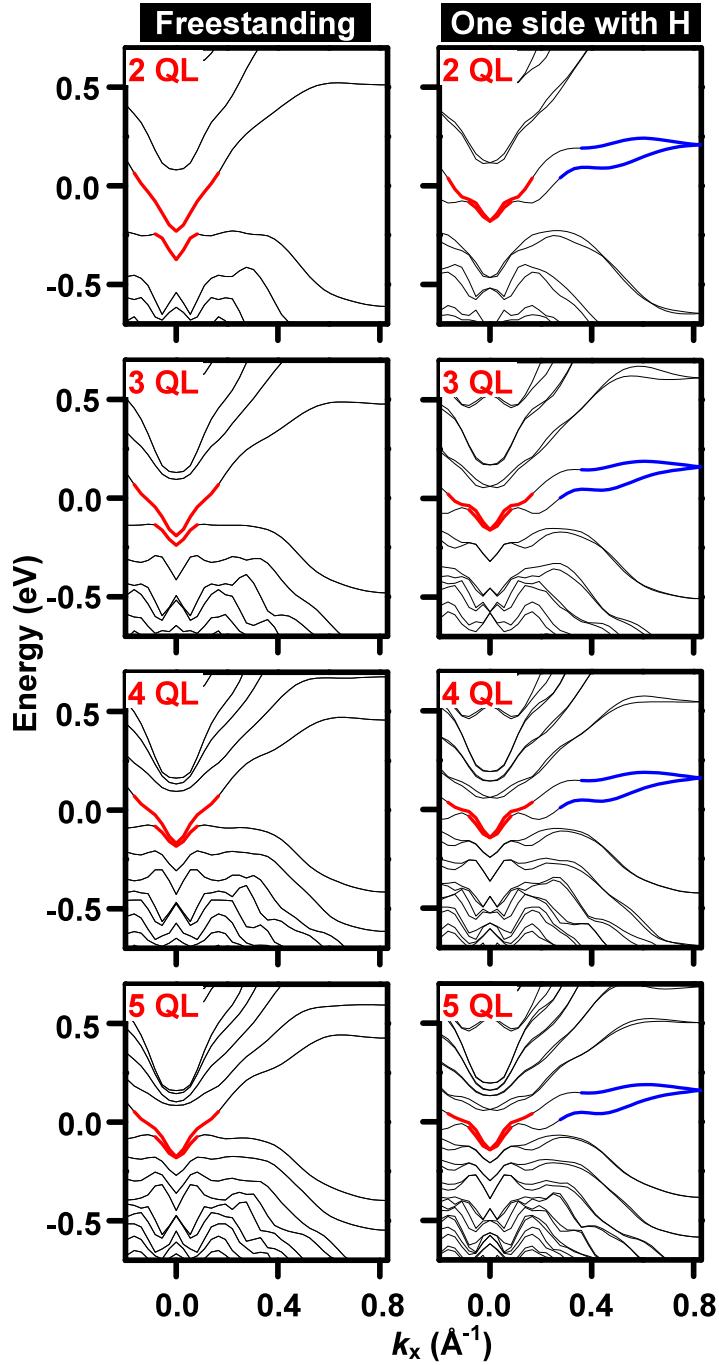


Fig. 6 (Color online). Band structures of 2-5 QL  $\text{Bi}_2\text{Te}_3$  films along the  $\bar{\Gamma}\bar{\text{M}}$  direction from first-principles calculations. Left panels: freestanding films; right panels: films with one side terminated by hydrogen. The red curves mark the topological surface states associated with the  $\text{Bi}_2\text{Te}_3$ -vacuum (top) surface, while the blue curves mark the topological surface states at the hydrogen-terminated (bottom) surface. Hydrogen bonding causes an energy shift of the TSSs at the bottom surface such that they no longer interact, by degenerate coupling, with the TSSs on the top surface.

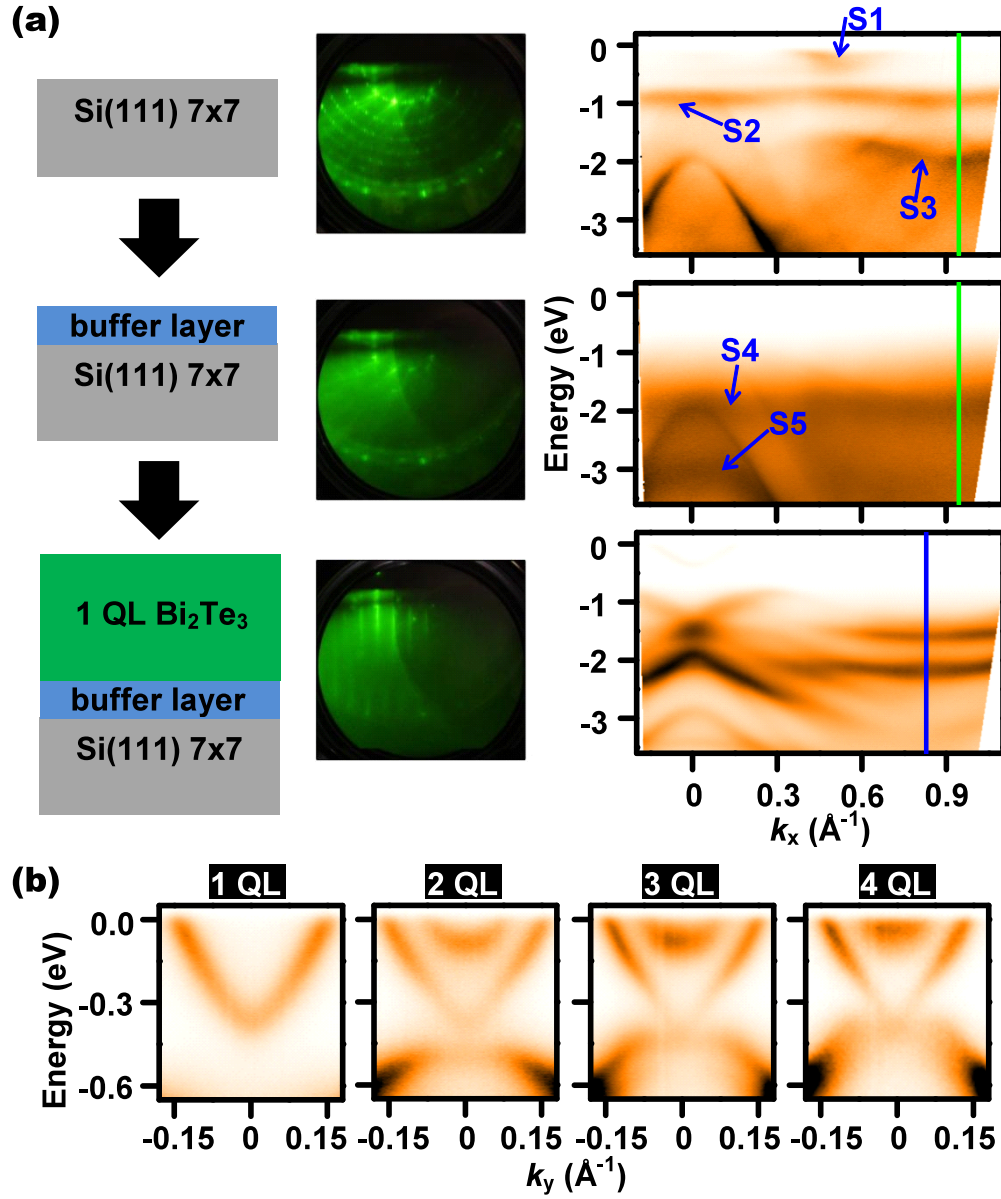


Fig. 7 (Color online). Evidence for quasi-freestanding  $\text{Bi}_2\text{Te}_3$  films. (a) A schematic diagram illustrating the proposed growth of quasi-freestanding  $\text{Bi}_2\text{Te}_3$  films via an intermediate buffer layer of Te which saturates all dangling bonds on the starting  $\text{Si}(111)-(7 \times 7)$  surface. The middle panels show the RHEED patterns at each stage and the right panels show the corresponding photoemission spectra taken with 24-eV photons. The green and blue vertical lines represent the  $\bar{M}$  point of Si and  $\text{Bi}_2\text{Te}_3$ , respectively. Surface states S1 – S5 are indicated. (b) Photoemission spectra of 1- through 4-QL films measured along  $\bar{\Gamma}\bar{K}$  using 26-eV photons. The warping effect is small along this direction.